Friction

Research Article

Wear evolution analysis of artificial joints based on wear particle recognition: A study under insufficient and imbalanced sample scenarios

Yeping Peng[1], Desheng Kong[1], Zihao Wang[1], Song Wang[2,✉], Chaozong Liu[3], Guang-Zhong Cao[1,✉]

Cite this article: Peng YP, Kong DS, Wang ZH, et al. *Friction* 2026, **14**: 9441236. https://doi.org/10.26599/FRICT.2026.9441236

ABSTRACT: Revealing the evolution law of wear conditions and mechanisms is critical for assessing the health status of artificial joints and thereby extending their service life. Notably, high-precision wear particle recognition plays a pivotal role in the intelligent wear analysis of joint implants. However, insufficient and imbalanced particle samples often lead to inadequate recognition accuracy, which fails to meet the requirements of reliable wear particle analysis. Such limitations highlight the urgent need for a robust solution to address sample scarcity and imbalance. To this end, an intelligent wear particle recognition method based on a generative adversarial network is proposed to enhance the accuracy of artificial joint wear analysis. Specifically, a multiscale coordinated attention-based generative adversarial network is designed to produce high-quality wear particle samples, which are used to supplement scarce sample categories and balance the particle distribution. Subsequently, a wear particle classifier is constructed using a neural network, and the training strategy for this classification model is further optimized to ensure high-precision wear particle recognition. Ablation experiments demonstrate that the proposed method achieves an accuracy, precision, recall, and F1-score of 0.90 for wear particle recognition when using the generated samples. All metrics represent a significant improvement compared with the results obtained from the original sample dataset. Meanwhile, the recognition performance of the proposed method outperforms that of other state-of-the-art algorithms. Based on the recognition results of wear particles from joint implants, the particle size and type distributions are derived to evaluate the wear evolution of artificial joints. These findings hold great value for advancing artificial joint wear analysis and enabling reliable failure prediction.

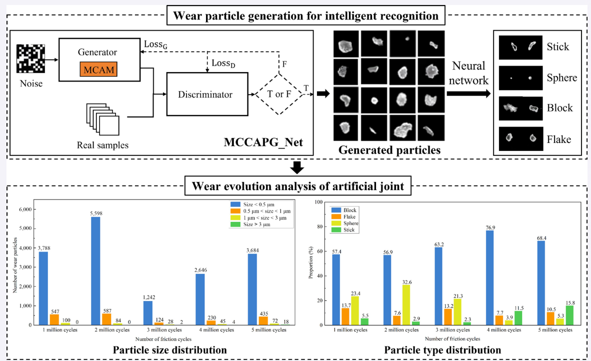

KEYWORDS: artificial joint; wear evolution analysis; wear particle recognition; generative adversarial network (GAN)

1 Introduction

Artificial joint replacement surgery has significantly increased in recent years because of the aging population and the early manifestation of joint diseases [1, 2]. Implanted joint prostheses need to adapt to the human environment and thus require meticulous consideration of various parameters, including biocompatibility, wear resistance, corrosion resistance, and elastic modulus. Biomedical materials, including cobalt–chromium–molybdenum (CoCrMo) alloys, ultrahigh molecular weight polyethylene (UHMWPE), cross-linked polyethylene (XLPE), and poly(ether ether ketone) (PEEK), have been widely used in clinical applications due to their superior biocompatibility and anti-friction properties [3–5]. However, prolonged reciprocating motion can cause surface wear between joint friction pairs, leading to loosening and failure of the joint implants [6–8]. Therefore, investigating the evolution of artificial joint wear conditions is significant for health assessment and performance improvement.

Wear particles are generated during the wear process of mechanical components, and their size and shape distributions serve as crucial characteristics for the intelligent identification of wear modes and wear status [9]. Correspondingly, wear particle analysis has been widely recognized as a reliable technology for assessing the wear condition of tribosystems [10–12]. In particular, the morphological characteristics of wear particles exhibit a strong correlation with specific wear mechanisms [13, 14]. For the purpose of analyzing the wear mechanisms of joint implants, wear particles are typically identified and classified

[1] Guangdong Key Laboratory of Electromagnetic Control and Intelligent Robots, College of Mechatronics and Control Engineering, Shenzhen University, Shenzhen 518060, China. [2] Biomechanics and Biotechnology Lab, Research Institute of Tsinghua University in Shenzhen, Shenzhen 518057, China. [3] Institute of Orthopaedics and Musculoskeletal Science, University College London, Royal National Orthopaedic Hospital, London HA7 4LP, UK.

✉ Corresponding authors. E-mail: S. Wang, wangs@tsinghua-sz.org; G.-Z. Cao, gzcao@szu.edu.cn

Received: October 20, 2025; Revised: January 8, 2026; Accepted: February 20, 2026

into four categories based on their shape: sphere, flake, stick, and block [15–17]. Specifically, spherical particles with residual subtle cutting scratches or indentations on the surface are occasionally observed in the stage of severe abrasive wear. Flake-shaped particles, characterized by their thin, lamellar structure, are mainly generated by fatigue spalling wear. Stick (rod-like) particles, featuring an elongated shape, are commonly linked to cutting wear. Block-shaped particles with rough surfaces and prominent scratch marks are predominantly associated with adhesive wear. Therefore, accurate recognition of wear particle types is critical for comprehensively analyzing the tribological behaviors and wear performance of friction pairs in joint implants [18–20].

To improve the recognition accuracy of wear particles, a variational mode decomposition (VMD) method was developed with a dual-filter intrinsic mode function to enhance the signals [21]. A novel hybrid convolutional neural network (CNN) model integrated with a Visual Geometry Group network, termed VRCNN [22], was designed to provide an automatic method for wear particle classification. TCBGY-Net [23] is a hybrid model for wear particle detection in ferrographic images that integrates a transformer, a convolutional block attention module (CBAM), a Ghost module, a bidirectional feature pyramid network (BiFPN), and you only look once version 5 (YOLOv5). It achieves a mean average precision (mAP@0.5) of 98.3%. Our previous work [15] also presented an intelligent method for moving wear particle recognition. The particle types could be effectively identified using the features acquired from multi-view image sequences at low resolution. However, the wear particles generated from artificial joints are much less abundant than those obtained from mechanical tribology systems. Furthermore, the capture of artificial joint wear particles is limited by complex separation operations and high-resolution scanning electron microscopy (SEM). These aspects result in an insufficient and imbalanced distribution of particle types, which may cause false detection and misdetection of the wear particles [17].

To address the issue of object recognition with insufficient and imbalanced samples, researchers have reported two main kinds of approaches: algorithmic and data-driven solutions [24]. Algorithmic solutions tackle the class imbalance through cost-sensitive learning, which modifies the training process by applying additional penalties to misclassified instances [25, 26]. Although algorithmic solutions can reduce the dependence on supplementary data, modification and refinement generally increase the complexity of the model [27]. Moreover, overfocusing on minority class samples during training may cause overfitting. These constraints impede the overall efficacy of algorithmic methodologies. Data-driven solutions focus on rebalancing class distributions by resampling algorithms [28]. Conventional resampling methods, such as Chawla's synthetic minority oversampling technique (SMOTE) [29], can generate synthetic samples to increase the quantity and diversity of minority class samples, thus improving classifier performance [30]. However, SMOTE's linear interpolation mechanism leads to the loss of texture, structural, and semantic details. Such deficiencies prevent synthetic samples from mimicking the true distribution of real data, ultimately restricting classifier generalization.

In recent years, generative adversarial networks (GANs) have been widely applied to generate high-fidelity samples to address the problem of class imbalance [31]. In particular, the integrated model combining GAN and CNN enables the discriminator to operate within a more semantically meaningful feature space, enhancing the quality of generated images and the efficiency of model training [32]. However, the receptive field of the local convolution operation is constrained by the kernel size. This constraint makes it challenging to effectively model long-range dependencies in images, leading to distortions or incoherences in the generated images, especially in regions that demand global consistency, such as complex textures and repetitive structures. To acquire correlation weights between different features, a self-attention mechanism is introduced into the GAN framework, namely, SAGAN [33], to adaptively focus on important information and capture long-range dependencies, improving the global consistency of generated images. However, the SAGAN performs self-attention computation at a single feature scale, which makes it difficult to capture feature information across multiple scales simultaneously. Owing to the size variability of wear particles, single-scale attention fails to adequately address both the overall morphological characteristics of large particles and the fine-grained details of small particles. Therefore, we integrate a multiscale coordinated attention module (MCAM) into a GAN-based framework to construct a wear particle generation model, denoted as MCCAPG_Net. Specifically, the MCAM is capable of capturing multiscale feature representations while modeling long-range dependencies, and then multilevel feature fusion through a cross-scale coordinated attention mechanism is achieved, ensuring both global consistency and fine-detail fidelity in the generated wear particle images. After sample generation, the particle features are extracted from a sufficient and balanced sample dataset for classification training by a neural network. During this stage, an optimization strategy is developed to improve the accuracy of wear particle recognition. Finally, the distribution of morphological characteristics is obtained based on the particle recognition results to analyze the wear evolution of joint implants. The main contributions are as follows:

(1) A new method for the wear evolution analysis of artificial joints is developed. The wear mechanism and wear status are revealed by the statistical distribution of wear particles. This method is designed to work effectively under sample-scarce conditions, addressing the practical challenge of limited particle acquisition in artificial joint monitoring.

(2) A generative adversarial network is optimized to generate wear particles to address the problems of insufficient and imbalanced samples. By generating high-quality particles that complement real samples, the particle recognition accuracy is significantly improved with balanced samples.

(3) A lightweight artificial neural network for wear particle recognition is constructed to ensure computational efficiency, which is particularly suitable for scenarios with limited sample resources. The integration of a learning rate annealing strategy and L2 regularization further enhances recognition accuracy.

2 Materials and methods

2.1 Experimental material and sample collection

Experiments were conducted using artificial knee joints to collect wear particle samples. The friction pairs of the joint prosthesis were made of CoCrMo alloys, PEEK, and XLPE. To accurately simulate the *in vivo* motion conditions of the joint prosthesis, the experimental parameters were set according to the total knee joint wear standard of ISO/AWI 14243-3 [34]. The experiments were conducted under 25% calf serum (CS) lubrication.

Since the experiments were conducted under 25% CS lubrication, acid decomposition and centrifugation methods were employed for wear particle separation and extraction to eliminate interference from proteins. Consequently, the extracted wear particles were predominantly XLPE particles. Afterwards, SEM was used to capture the particle images at the micro- and nanoscales, as shown in Fig. 1(a). To eliminate background interference and facilitate efficient feature extraction, the wear particles were segmented from image backgrounds. Particle segmentation can be implemented with deep learning algorithms, including U-Net [17], hybrid CNN [18], and our previously proposed wear particle detection and recognition network (WP-DRnet) [19]. In this work, the WP-DRnet was adopted for particle segmentation. A total of 1,267 wear particle samples were annotated, where 1,014 samples were allocated for training and 253 for testing. The segmented wear particles are displayed in Fig. 1(b). The average segmentation precision reaches 0.88, with errors primarily attributed to the irregular and blurred contours of certain particles.

2.2 Wear particle generation

2.2.1 Methodology

The collected wear particles (real samples) are used to generate simulation samples. The MCCAPG_Net is designed to generate high-quality particle samples to balance the distribution of wear particle types, and its framework is illustrated in Fig. 2. The GAN model is employed as the baseline model, in which the generator and discriminator networks compete to produce high-quality samples. However, traditional GANs often become unstable when generating images with resolutions exceeding 96 pixels × 96 pixels, leading to noticeable discrepancies between the generated and original images. To address this issue, the MCAM is integrated in the generation network to expand the receptive field and enhance the integration of contextual information, ensuring that the model focuses on the most relevant features when processing data. The discrimination network incorporates residual coupling modules and stacked residual blocks, adopting a quasi-residual structure to extract deep local features and improve feature extraction capabilities. Finally, a joint loss function is designed to balance the training stability of MCCAPG_Net with the quality of the generated samples.

As shown in Fig. 2(b), the MCAM consists of a multiscale fusion module (MFM) and a global spatial attention module (GSAM). The MFM is used to capture and process multiscale semantic information and intricate details within the input feature maps. The GSAM encodes and models spatial feature information, calculating and coordinating the relationships between pixel features via a self-attention mechanism. By integrating MFM with GSAM, the proposed framework realizes a full-dimensional feature representation that simultaneously preserves fine-grained texture details and maintains global structural consistency, thereby facilitating the generation of high-quality wear particle images.

The principle of MFM is as follows. Initially, the input feature maps undergo preliminary processing through a neck network, which is composed of a 3 × 3 convolutional layer with a stride of 1 to maintain the image details, a batch normalization (BN) layer, and the leaky rectified linear unit (ReLU) activation function. Subsequently, dilated convolutions with dilation rates of 2, 4, and 8 are applied to extract feature regions by performing weighted summation over multiple neighboring features, expanding the receptive field to facilitate the efficiency of feature extraction. Next, global average pooling is applied to the feature maps in the parallel branches, aggregating multireceptive field information to adaptively integrate feature parameters across different receptive field scales. Finally, residual connections concatenate the feature maps from the neck network output with those from the global average pooling operation, and the sigmoid function is applied to produce the final feature weight map.

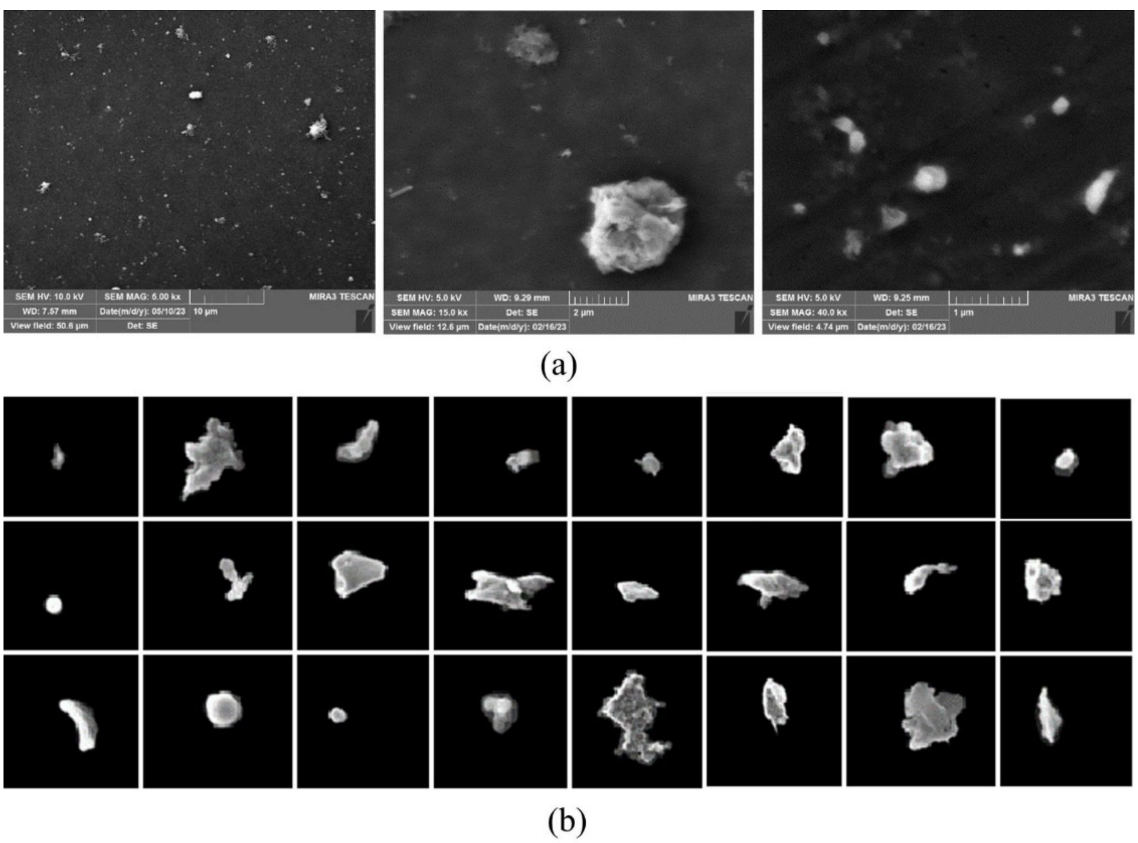

Fig. 1 SEM images of wear particles and their segmentation results: (a) SEM images of wear particles and (b) wear particle segmentation results.

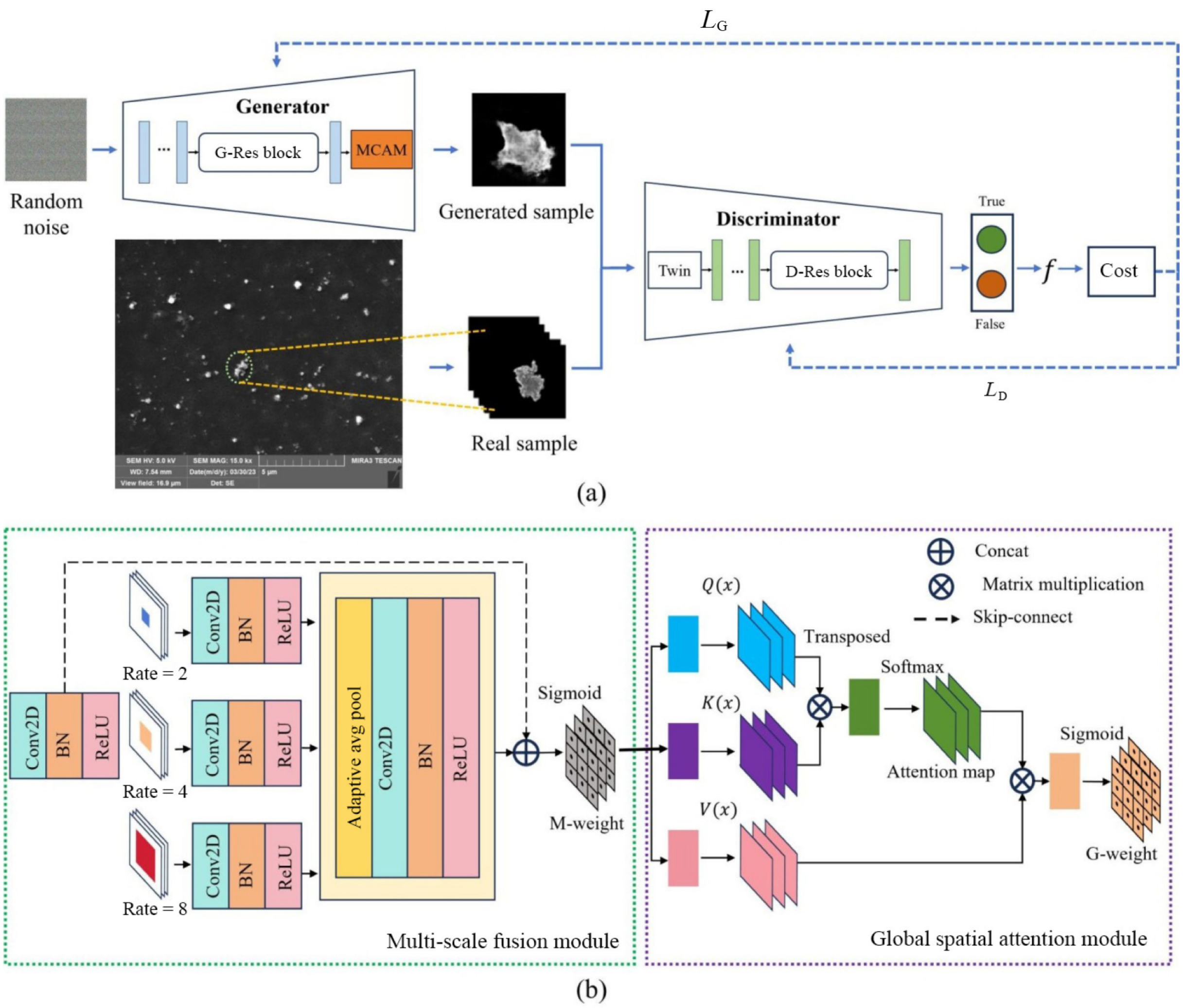

Fig. 2 Framework of proposed wear particle generation network (MCCAPG_Net): (a) main network framework and (b) structure of MCAM.

The GSAM is defined as follows. Let the feature map from the previous layer be denoted as $X=\{x_i\}, i=1, 2, \ldots, N_p$. The attention score $\zeta_{i,j}$ of pixel position j with respect to pixel position i is calculated as Eqs. (1)–(5):

$$Q(x)=K_qX\in\mathbb{R}^{H\times W\times N_c} \tag{1}$$

$$K(x)=K_kX\in\mathbb{R}^{H\times W\times N_c} \tag{2}$$

$$V(x)=K_vX\in\mathbb{R}^{H\times W\times N_c} \tag{3}$$

$$\zeta_{j,i}=\frac{\exp\left(Q_i^{\mathrm{T}}K_j\right)}{\sum_{i=1}^{N_p}\exp\left(Q_i^{\mathrm{T}}K_j\right)} \tag{4}$$

$$O_j=K_s\left(\sum_{i=1}^{N_p}\zeta_{j,i}V_i\right) \tag{5}$$

where Q, K, and V denote the outputs shown in Fig. 2(b); H and W are the height and width of the feature map, respectively; N_c and N_p are the number of channels and pixels, respectively; K_q, K_k, K_v, and K_s represent the convolution kernels; O represents the output of the GSAM. Finally, the feature maps produced by the MCAM are passed through the tanh activation function to generate high-quality wear particle samples.

The Wasserstein GAN (WGAN) [35] uses the Wasserstein distance to measure the similarity between the distributions of real and generated samples. This approach provides smoother gradients for the model, effectively mitigating the issues of gradient vanishing and gradient explosion. The objective function of the WGAN is defined as Eq. (6):

$$F=\arg\min_{G}\max_{f_\omega\in K-\text{Lipschitz}}\left(\mathbb{E}_{x\sim pr(x)}f_\omega(x)-\mathbb{E}_{z\sim pg(z)}f_\omega(G(x))\right) \tag{6}$$

where f_ω is a parameterized function that satisfies the $K-$Lipschitz condition and $\mathbb{E}_{\boldsymbol{x}\sim pr(\boldsymbol{x})}f_\omega(x)$ and $\mathbb{E}_{\boldsymbol{z}\sim pg(\boldsymbol{z})}f_\omega(G(x))$ represent the expected values of the real sample $\boldsymbol{x}$ and generated sample $G(x)$, respectively. The loss functions for the generator (L_{WG}) and discriminator (L_{WD}) are expressed as Eqs. (7) and (8):

$$L_{\text{WG}}=-\frac{1}{N_s}\sum_{i=1}^{N_s}D(G(x_i)) \tag{7}$$

$$L_{\text{WD}}=-\frac{1}{N_s}\sum_{i=1}^{N_s}\left(D(x_i)-D(G(x_i))\right) \tag{8}$$

where $D(x_i)$ and $D(G(x_i))$ represent the discriminator scores for real samples and generated samples, respectively; N_s denotes the number of samples.

Geometric GAN [36] adopts a geometric interpretation and loss function similar to that of a support vector machine (SVM), encouraging the discriminator network to learn a well-defined decision boundary that distinctly separates real samples from generated ones. This helps the generator network better approximate the distribution of real data. Therefore, this study introduces hinge loss as the loss function for the network, which is expressed as Eqs. (9) and (10):

$$L_{\mathrm{HG}} = -\frac{1}{N_{\mathrm{s}}}\sum\nolimits_{i=1}^{N_{\mathrm{s}}} D(G(x_i)) \tag{9}$$

$$L_{\mathrm{HD}} = \frac{1}{N_{\mathrm{s}}}\sum\nolimits_{i=1}^{N_{\mathrm{s}}} \max(0,1-D(x_i)) + \frac{1}{N_{\mathrm{s}}}\sum\nolimits_{i=1}^{N_{\mathrm{s}}} \max(0,1+D(G(x_i))) \tag{10}$$

where L_{HG} and L_{HD} represent the loss functions of the generator and discriminator in the geometric GAN, respectively.

This work combines hinge loss with the Wasserstein distance to form a weighted loss function. By adjusting the weight parameters, a balance is achieved between the training stability of the MCCAPG_Net model and the quality of the generated samples. The loss functions for the generator (L_{G}) and discriminator (L_{D}) are expressed as Eqs. (11) and (12):

$$L_{\mathrm{G}} = \alpha L_{\mathrm{WG}} + \beta L_{\mathrm{HG}} \tag{11}$$

$$L_{\mathrm{D}} = \alpha L_{\mathrm{WD}} + \beta L_{\mathrm{HD}} \tag{12}$$

where α and β are both hyperparameters, which were determined through grid search and contrastive experiments. A series of contrastive experiments were performed with different weight ratio configurations, and the results demonstrate that the parameter setting of α:β = 0.5:0.5 achieves the optimal wear particle generation accuracy.

2.2.2 Evaluation metrics

Six evaluation metrics were employed to evaluate the performance of the particle generation network: structural similarity (SSIM), variance of Laplacian (VoL), one-dimensional image entropy (Ent_1), spatial frequency (SF), image availability (IA), and Fréchet inception distance (FID). SSIM is used to measure the similarity between two images. VoL is used to evaluate the sharpness of the image by assessing the richness or dispersion of edge information in the wear particle images. Ent_1 can reveal the amount of information contained in the aggregation characteristics of the grayscale distribution in the wear particle images. SF is used to describe the rate of change of the grayscale values with respect to spatial position, where a higher rate of spatial change indicates better and sharper image quality. IA is used to measure the proportion of usable samples in a set of samples, reflecting the usability and reliability of the generation model. FID is adopted to measure the statistical similarity between the distributions of real and generated images. Their expressions are as given by Eqs. (13)–(20):

$$\mathrm{SSIM}(\mathrm{h},\mathrm{s}) = \frac{(2\mu_{\mathrm{h}}\mu_s + C_1)(2\sigma_{\mathrm{hs}} + C_2)}{(\mu_h^2 + \mu_s^2 + C_1)(\sigma_h^2 + \sigma_s^2 + C_2)} \tag{13}$$

where h and s represent the original image and the generated image, respectively; μ_{h} and μ_{s} denote the mean values of the original and generated images, respectively; σ_{h} and σ_s represent their respective standard deviations; $2\sigma_{\mathrm{hs}}$ refers to the covariance between the two images; C_1 and C_2 are constants.

$$\mathrm{VoL} = \frac{\partial^2 f}{\partial^2 x} + \frac{\partial^2 f}{\partial^2 y} \tag{14}$$

where $(\partial^2 f)/(\partial^2 x)$ and $(\partial^2 f)/(\partial^2 y)$ represent the second-order derivatives of the image along the horizontal and vertical axes, respectively, calculated using the Sobel operator. By summing these derivatives, the Laplacian operator is obtained.

$$\mathrm{Ent}_1(x) = \sum\nolimits_i P(x_i) I(x_i) = -\sum\nolimits_i P(x_i)\log_2 P(x_i) \tag{15}$$

where $P(x_i)$ represents the proportion of pixels with a grayscale of x_i.

$$\mathrm{RF} = \frac{1}{\sqrt{(M-1)(N-1)}}\sum\nolimits_{i=1}^{M-1}\sum\nolimits_{j=1}^{N-1}(g(i,j) - g(i,j+1))^2 \tag{16}$$

$$\mathrm{CF} = \frac{1}{\sqrt{(M-1)(N-1)}}\sum\nolimits_{i=1}^{M-1}\sum\nolimits_{j=1}^{N-1}(g(i,j) - g(i+1,j))^2 \tag{17}$$

$$\mathrm{SF} = \sqrt{\mathrm{RF}^2 + \mathrm{CF}^2} \tag{18}$$

where RF and CF denote the row frequency and column frequency of the particle image, respectively, and M and N represent the image width and height, respectively.

$$\mathrm{IA} = \frac{N_{\mathrm{u}}}{N_{\mathrm{g}}} \tag{19}$$

where N_{u} represents the total number of usable images and N_{g} is the total number of generated samples.

$$\mathrm{FID} = ||A_X - A_Y||_2^2 + \mathrm{tr}\left(E_X + E_Y - 2\sqrt{E_X E_Y}\right) \tag{20}$$

where A_X and A_Y are the feature mean vectors of real images and generated images, respectively; $||\cdot||_2^2$ is the squared Euclidean distance; E_X and E_Y refer to the feature covariance matrices of real images and generated images, respectively; $\mathrm{tr}(\cdot)$ represents the trace of a matrix.

2.3 Wear particle recognition

2.3.1 Methodology

In scenarios with insufficient samples, it is challenging for end-to-end deep learning methods to automatically extract deep features for high-performance wear particle recognition, as they are inherently dependent on large-scale training datasets. On the basis of the segmented and generated particle samples, it is easy to acquire the particle morphologies of shape and texture features. By doing so, a multiple classifier of artificial neural networks is suggested to recognize the particle types to ensure efficiency. Meanwhile, this approach can avoid extensive sample labeling and training times. Considering the shape characteristics of artificial joint wear particles, including spheres, flakes, sticks, and blocks, we select eight feature parameters, namely, roundness (R), aspect ratio (AR), irregularity (IR), concavity (C), rectangularity (Re), angular second moment (ASM), contrast (Con), and entropy (Ent), for particle recognition. Their definitions and mathematical expressions are presented in Table 1. This is because sphere and stick particles can be identified using roundness and aspect ratio features, while flake and block particles should be distinguished by their surface texture features [15, 37, 38].

The structure for the neural network of wear particle recognition is shown in Fig. 3. Key hyperparameters (number of hidden layers, neurons per layer, and training epochs) were optimized via a full-factorial experimental design. Experimental

Table 1 Definition of wear particle features and their expressions

Parameter	Definition	Expression
R	Degree of similarity between wear particle and a circle	$\frac{4A}{\pi P^2}$
AR	Ratio of wear particle length to its width	$\frac{L_p}{W_p}$
IR	Complexity and irregularity of wear particle contour	$2\pi\left(\frac{\sqrt{A}}{P}-\sqrt{\frac{{L_p}^2+{W_p}^2}{2L_pW_p}}\right)$
C	Degree of concavity on the wear particle surface	$\frac{Z}{A}$
Re	Degree of similarity between wear particle and a rectangle	$\frac{A}{L_pW_p}$
ASM	Homogeneity and roughness of wear particle texture	$\sum_i\sum_j(g(i,j))^2$
Con	Sharpness and depth of the grooves in wear particle surface	$\sum_i\sum_j(i-j)^2g(i,j)$
Ent	Degree of randomness and complexity of wear particle texture	$-\sum_i\sum_j g(i,j)\log_2 g(i,j)$

A: particle area; P: perimeter of particle contour; L_p and W_p: particle length and width, respectively; Z: perimeter of convex hull; $g(i, j)$: grayscale value of the image pixel at coordinate (i, j).

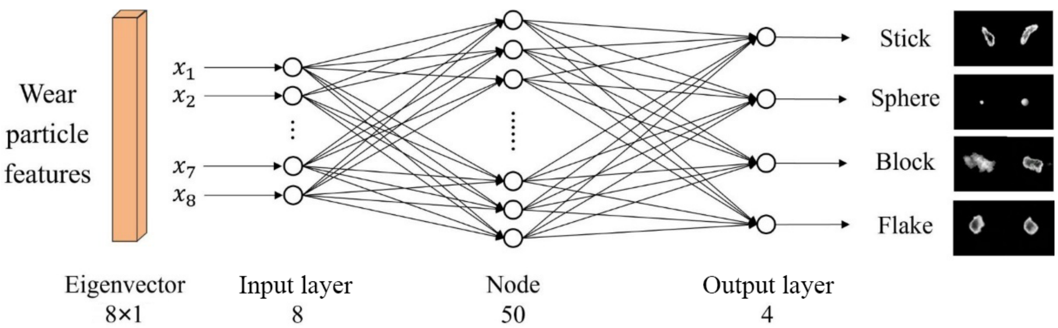

Fig. 3 Structure of constructed neural network model.

results demonstrate that this configuration (1 hidden layer, 50 neurons per hidden layer, and 100 training epochs) achieves the best performance in terms of comprehensive metrics such as accuracy and F1-score. The selected particle features are combined into an 8 × 1 feature vector and used as input. To improve the recognition accuracy, an optimization strategy is suggested to enable the model to effectively integrate various features. For this purpose, the initialization method by He et al. [39] (He initialization) is employed to adaptively adjust the initial weights of the model, which helps to maintain the stability of the gradient between intermediate layers.

For each layer, the weights are randomly drawn from a normal distribution, which is expressed by Eq. (21):

$$W_e \sim \aleph\left(0, \frac{2}{f_{out}}\right) \tag{21}$$

where W_e is the model weight and f_{out} represents the number of output neurons in the corresponding layer.

Furthermore, a cosine annealing learning rate strategy is introduced to balance training speed and model stability. A higher learning rate is preset to accelerate model convergence. During the training process, the learning rate is gradually reduced to fine-tune the network's weights. When the learning rate decreases to a preset threshold, it is increased again to allow the model to escape potential local optima. The mathematical expression for the learning rate (η) is given by Eq. (22):

$$\eta = \eta_{min} + \frac{1}{2}(\eta_{max} - \eta_{min})\left(1 + \cos\left(\frac{T_{cur}}{T_{max}}\pi\right)\right) \tag{22}$$

where η_{min} and η_{max} are the preset minimum and maximum learning rates, respectively, and T_{cur} and T_{max} are the current and maximum iteration numbers, respectively.

To ensure the ability of wear particle recognition, the focal loss is adopted as the loss function of the network model. This is because the focal loss can enhance the classification accuracy on difficult-to-recognize particles by adjusting the contribution of different kinds of samples to the overall loss. The mathematical expression for the focal loss function is given by Eq. (23):

$$\text{Loss}_{focal} = -\alpha_t(1-P_t)^{\gamma}\ln P_t \tag{23}$$

where P_t represents the predicted probability of the true class, α_t is an optional weighting factor used to balance positive and negative samples, and γ is a hyperparameter that adjusts the weighting factor. To avoid overfitting, the focal loss function incorporates an L2 regularization term. The mathematical expression is given by Eq. (24):

$$\text{Loss}'_{focal} = -(1-P_t)^{\gamma}\ln P_t + \frac{\lambda}{2N_t}||W||^2 \tag{24}$$

where $||W||^2$ represents the L2 norm of the model weight; N_t is the number of training samples; λ is set to control the weight of the L2 regularization term.

2.3.2 Evaluation metrics

The metrics of accuracy, precision, recall, and F1-score are employed to evaluate the performance of wear particle recognition. Their expressions are given by Eqs. (25)–(28):

$$\text{Accuracy} = \frac{\text{TP} + \text{TN}}{\text{TP} + \text{TN} + \text{FP} + \text{FN}} \tag{25}$$

$$\text{Precision} = \frac{\text{TP}}{\text{TP} + \text{FP}} \tag{26}$$

$$\text{Recall} = \frac{\text{TP}}{\text{TP} + \text{FN}} \tag{27}$$

$$\text{F1-score} = \frac{2\times\text{Precision}\times\text{Recall}}{\text{Precision} + \text{Recall}} \tag{28}$$

where TP denotes the number of particles belonging to the positive type that are correctly recognized; TN represents the number of particles belonging to the negative type that are correctly recognized; FP refers to the number of particles belonging to the negative type that are misrecognized; FN is the number of particles belonging to the positive type that are misrecognized.

3 Results and discussion

3.1 Evaluation of the particle generation network

To evaluate the performance of the developed particle generation network, a total of 625 wear particles were collected and used as real samples, which contained 403 block, 162 flake, 47 stick, and 13 sphere particles. The resolution of particle images was set to 128 pixels × 128 pixels.

3.1.1 Ablation experiment

A contrastive experiment was conducted with the baseline network of MCCAPG_Net, the residual block (ResBlock) [40], MCAM, and the twin module [41], which can be seen in Fig. 2. The baseline network comprises six two-dimensional (2D) convolutional layers with kernel sizes of 4 × 4 and strides of [1, 2, 2, 2, 2, 2]. These hyperparameters were initially configured based on experience and optimized through 5-fold cross-validation to balance model accuracy and computational efficiency. To verify the effectiveness of each module in MCCAPG_Net, a total of 6 group ablation experiments were designed as follows.

(1) Group #1: Only the baseline network of MCCAPG_Net was performed.

(2) Group #2: The 2D convolution layers in the baseline network were replaced by the ResBlock to evaluate the gain provided by the ResBlock.

(3) Group #3: The ResBlock and the MCAM were combined with the baseline network for sample generation.

(4) Group #4: The twin module was integrated into the discriminator module, while the MCAM was not included in the generation module.

(5) Group #5: The twin module was integrated into the discriminator module, and the generation module contained the MCAM.

(6) Group #6: The hinge loss function was replaced by the designed joint loss function to verify the effectiveness of the proposed network.

The particle generation results of different group experiments are shown in Fig. 4, and the performance metric values are listed in Table 2. It can be seen from the results of group #1 that the central regions of the generated particles are missing. After introducing the ResBlock (group #2), the local details of the particles are captured. Accordingly, the SSIM increases to 0.92. However, the error edge textures lead to increases in FID (27.13) and decreases in other factors. From the results of groups #3 and

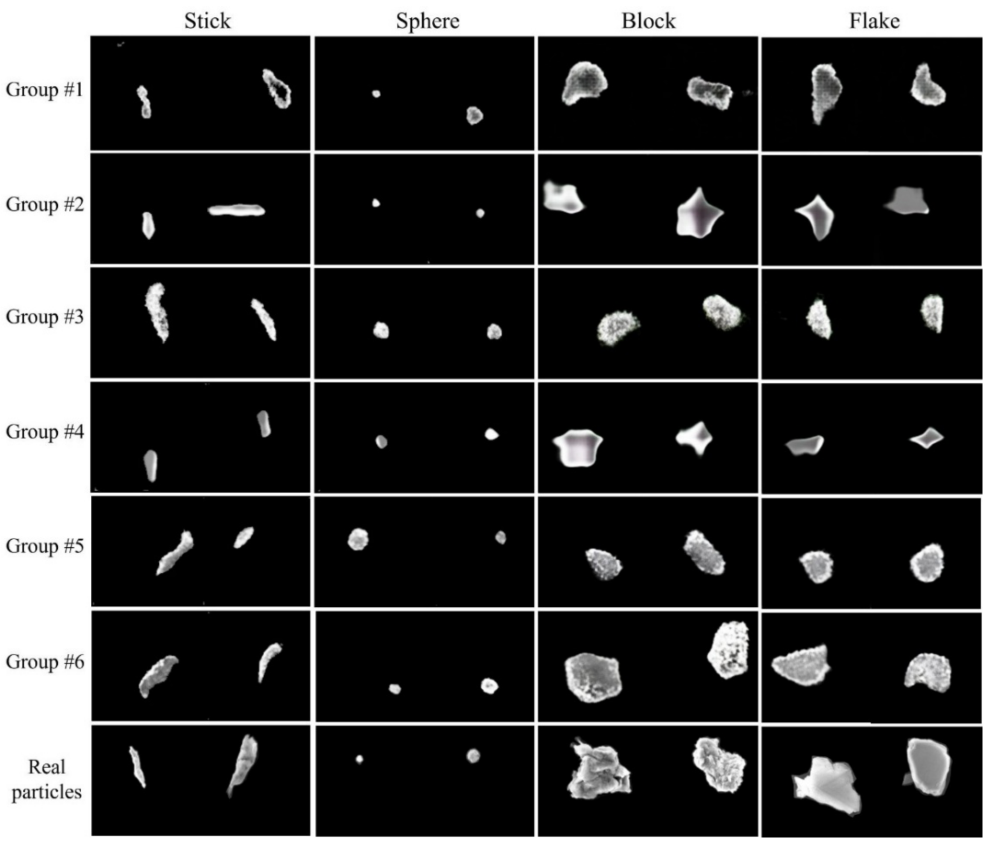

Fig. 4 Particle generation results of different group experiments.

Table 2 Performance metric values of generation network with different structures

Group	Baseline	Res	MCAM	Twin	Hinge	Joint loss	SSIM	Ent_1	VoL	SF	IA	FID
#1	√	×	×	×	√	×	0.89	1.18	309.12	13.42	0.65	24.41
#2	√	√	×	×	√	×	0.92	0.73	205.04	12.00	0.19	27.13
#3	√	√	√	×	√	×	0.93	0.73	252.26	11.86	0.90	25.22
#4	√	√	×	√	√	×	0.93	0.66	184.76	11.35	0.17	27.01
#5	√	√	√	√	√	×	0.92	0.74	230.40	12.06	0.23	23.68
#6 (proposed)	√	√	√	√	×	√	0.98	0.97	333.75	13.88	0.80	22.70

#4, the MCAM module outperforms the twin module across four key metrics, achieving higher values for Ent_1 (0.73), VoL (252.26), SF (11.86), and IA (0.90). The lower FID (25.22) also indicates higher-quality particle generation by utilizing the MCAM module. This is because the MCAM module can capture more discriminative texture details to support high-fidelity wear particle generation, which can be seen in the feature heatmaps shown in Fig. 5. The heatmaps demonstrate that the MCAM precisely localizes core particle regions (highlighted in yellow) while emphasizing critical details such as striated surfaces (marked in red). This confirms that the MCAM effectively balances the extraction of global particle contours and local edge features for wear particle generation.

After combining the MCAM and twin modules (group #5), smoother transition of the detailed texture is achieved, promoting increases in Ent_1 (0.74) and SF (12.06). However, the VoL (230.40) and IA (0.23) are significantly decreased, which may be caused by model instability. Comparing the results of groups #5 and #6, we observe that more contour textures are generated from the proposed MCCAPG_Net with the designed joint loss function. The SSIM (0.98), Ent_1 (0.97), VoL (333.75), SF (13.88), and IA (0.80) of the proposed method are the highest among the experimental groups. Specifically, the lowest FID (22.70) indicates that the proposed method can provide similar wear particle samples for further analysis.

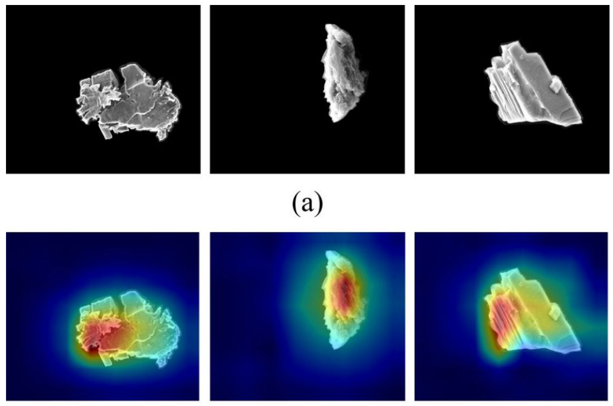

(a)

(b)

Fig. 5 Feature heatmaps for visualized analysis of MCAM: (a) input particle images and (b) feature heatmaps of MCAM.

3.1.2 Comparison experiment

To evaluate the performance of the proposed particle generation network, a comparison experiment was conducted with the designed MCCAPG_Net and four mainstream generation networks of SAGAN [42], ProGAN (progressive growing GAN) [43], and StyleGAN3 (alias-free generative adversarial network) [44]. The particle generation results of different networks are shown in Fig. 6. The quantitative evaluation results are listed in Table 3. The proposed particle generation model, MCCAPG_Net, achieves the best performance (SSIM of 0.98, SF of 13.88, IA of 0.80, and FID of 22.70) among the networks. Although StyleGAN3 shows higher Ent_1 (1.39) and VoL (359.01), its lower SSIM (0.91) and SF (13.84) indicate that the structure information is missing. Edge distortion on the generated wear particles from StyleGAN3 is shown in Fig. 6(c). The wear particles generated by MCCAPG_Net have clearer structural features, as shown in Fig. 6(d). This indicates that our proposed method is more suitable for generating and balancing the wear particle samples of artificial joints.

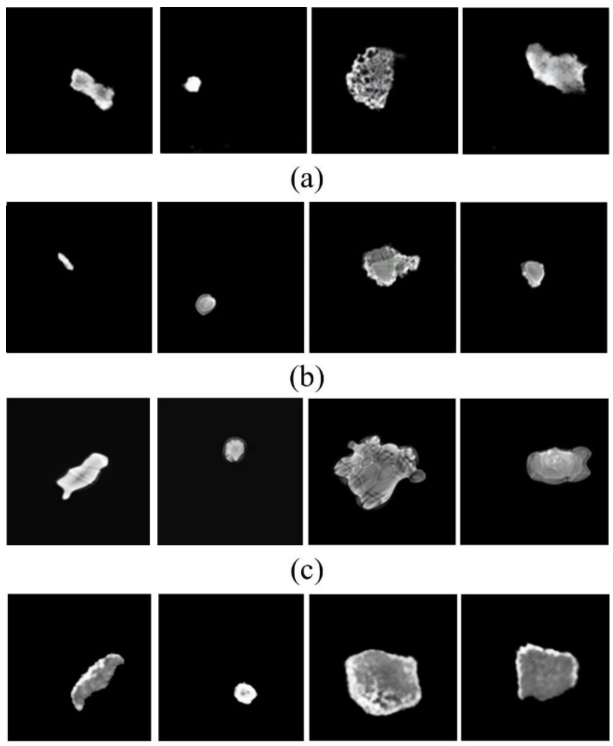

(a)

(b)

(c)

(d)

Fig. 6 Wear particle generation results obtained from different networks: (a) SAGAN, (b) ProGAN, (c) StyleGAN3, and (d) MCCAPG_Net.

3.2 Evaluation of the particle recognition model

To evaluate the proposed particle recognition model, 331 particles were selected as the original training set and 294 as the test set. This nearly balanced split was configured to ensure test set consistency across all experiments, including baseline model assessment and validation with MCCAPG_Net-generated augmented training samples. The fixed test set comprehensively covers four particle types (block, flake, stick, and sphere) with adequate per-class representation, eliminating test set variability as a confounding factor and enabling direct, unbiased performance comparisons between models. A total of 832 particles were generated by MCCAPG_Net, evenly distributed across the four categories with 208 samples per particle type. The distribution of wear particle types across the training and test sets is shown in Table 4.

3.2.1 Ablation experiment

To verify the effectiveness of the constructed wear particle recognition model, an ablation experiment was conducted with 7 models configured with different activation and loss functions, as shown in Table 5. Model #1 serves as the baseline, adopting the traditional cross-entropy (CE) loss function. To mitigate class imbalance, model #2 replaces CE loss with focal loss. Building on model #2, models #3–5 incorporate the He initialization [39] and a cosine annealing learning rate schedule. Further extending this framework, model #6 introduces L2 regularization to evaluate its impact on recognition performance. Model #7 leverages the generated particle samples to verify the efficacy of the wear particle generation network.

To quantitatively analyze the performance of different recognition models, the evaluation metrics of accuracy, precision, recall, and F1-score are calculated and listed in Table 5. Focal loss is more suitable for addressing class imbalance compared with CE loss, obtaining higher accuracy (0.77) for model #2 than that for model #1 (0.76). The proposed optimization strategy combining cosine annealing and L2 regularization (model #6) effectively improves the particle recognition accuracy (0.79). After extending the particle samples to balance the distribution of different types, the particle recognition accuracy (0.90) is significantly improved, and the F1-score is the highest, reaching 0.90. This indicates that the proposed intelligent method is satisfactory in addressing the issue of recognizing artificial joint wear particles with insufficient and imbalanced samples.

3.2.2 Comparison experiment

To further evaluate the method performance, a comparison experiment was conducted with traditional machine learning algorithms, including K-nearest neighbors (K-NN) and random forest. Considering the remarkable performance of TCBGY-Net [23] in wear particle detection, it was also selected as a comparative method. The wear particle recognition results obtained from different algorithms are shown in Fig. 7. The particle types are color-coded in Fig. 7(b). Figure 7(c) shows that all algorithms show recognition errors using the original sample dataset. After extending the particle samples, the recognition accuracies of all algorithms are significantly improved, as shown in Fig. 7(d).

The quantitative indices of accuracy, precision, recall, and F1-score of different recognition algorithms are shown in Table 6. The accuracies of all algorithms are less than 0.80 when performed with the original sample dataset. After expanding the dataset using the generated samples, the accuracies of all algorithms are significantly improved and larger than 0.85. In contrast, the proposed method provides the highest accuracy, precision, recall, and F1-score, and all of the values reach 0.90. It can also be seen that the accuracy of the deep learning model extremely depends on the sample quantity. The F1-score of TCBGY-Net increases from 0.53 to 0.89 after sample expansion. Figure 7(d) shows that recognition errors of small particles are produced from TCBGY-Net. This is because the network was trained using the generated particle images without manual labels. Considering the influence of the image background, more training samples are needed to improve the particle recognition accuracy.

For further analysis, the category-specific recognition accuracies of particle types across different classifiers are presented in Table 7. When the original imbalanced sample dataset was used for testing, the recognition accuracy of different types of wear particles was also highly imbalanced: The recognition rate for the under sampled sphere and stick particles dropped to 0. After dataset balancing, the recognition accuracy of these two categories increased significantly, with the accuracy reaching 100% for some cases. It is also worth noting that the recognition accuracy of block particles did not improve with the increase in their quantity,

Table 3 Evaluation metric values of different generation networks

Network model	SSIM	Ent_1	VoL	SF	IA	FID
SAGAN	0.89	0.88	309.12	12.88	0.76	35.46
ProGAN	0.93	0.64	282.98	12.02	0.78	34.66
StyleGAN3	0.91	1.39	359.01	13.84	0.80	27.01
MCCAPG Net	0.98	0.97	333.75	13.88	0.80	22.70

Table 4 Distribution of wear particle types

Wear particle type	Block	Flake	Stick	Sphere	Overall
Original training sample	208	96	17	10	331
Augmented training sample	208	208	208	208	832
Testing sample	195	66	30	3	294

Table 5 Performance metric values of particle recognition network with different structures

Model	He initialization	Annealing strategy	Focal loss	CEloss	L2	Generated samples	Accuracy	Precision	Recall	F1-score
#1	×	×	×	√	×	×	0.76	0.75	0.84	0.79
#2	×	×	√	×	×	×	0.77	0.76	0.87	0.81
#3	√	×	√	×	×	×	0.78	0.76	0.87	0.81
#4	×	√	√	×	×	×	0.78	0.77	0.86	0.81
#5	√	√	√	×	×	×	0.78	0.79	0.88	0.83
#6	√	√	√	×	√	×	0.79	0.79	0.88	0.83
#7	√	√	√	×	√	√	0.90	0.90	0.90	0.90

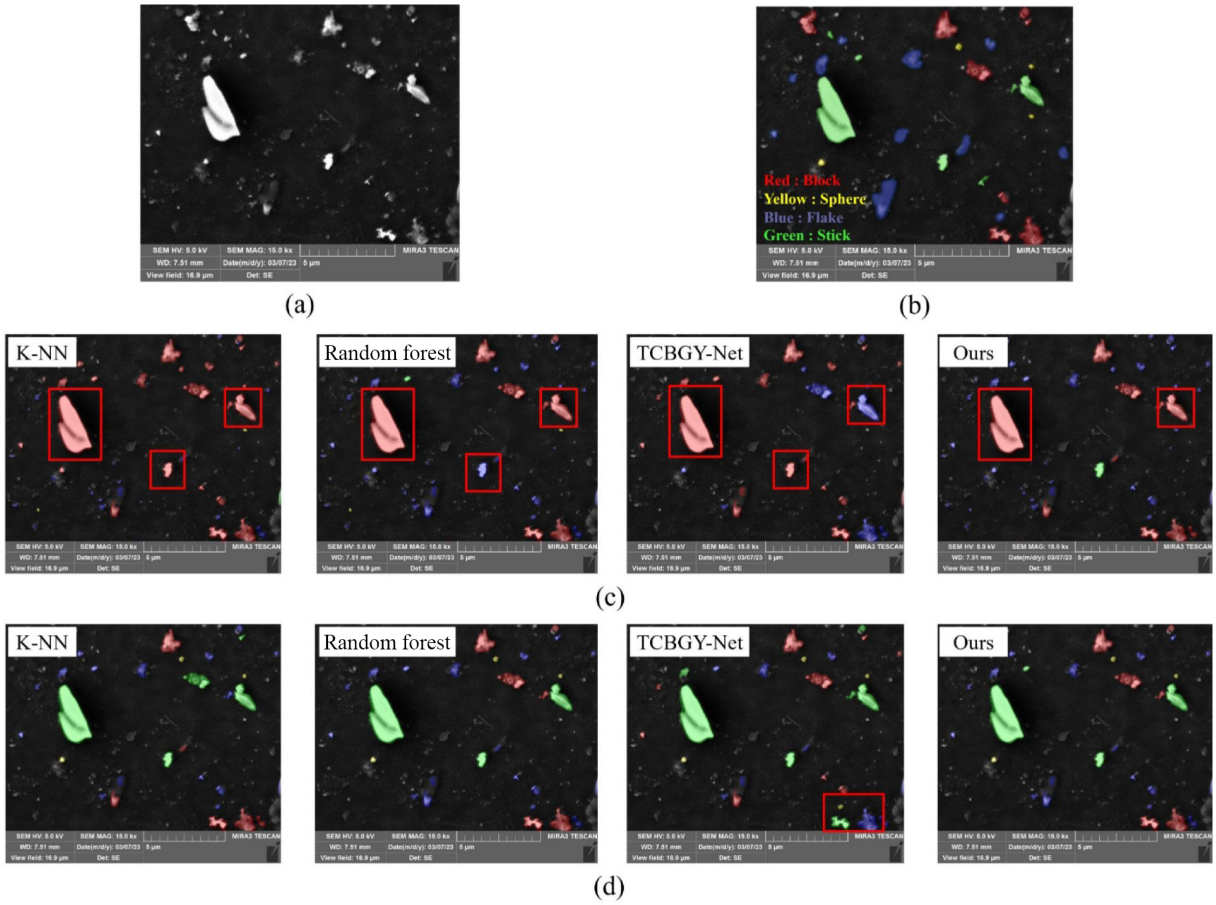

Fig. 7 Wear particle recognition results obtained from different algorithms: (a) captured image, (b) target particles labeled with colors, (c) particle recognition results of different algorithms using original sample dataset, and (d) particle recognition results of different algorithms using expanded sample dataset.

Table 6 Performance comparison with existing classifiers

Algorithm	Original dataset				Original dataset+generated dataset			
	Accuracy	Precision	Recall	F1-score	Accuracy	Precision	Recall	F1-score
K-NN	0.74	0.72	0.87	0.79	0.85	0.84	0.88	0.86
Random forest	0.76	0.75	0.88	0.81	0.87	0.87	0.87	0.87
TCBGY-Net	0.66	0.57	0.56	0.53	0.86	0.88	0.90	0.89
Proposed	0.79	0.79	0.88	0.83	0.90	0.90	0.90	0.90

Table 7 Category-specific recognition accuracies of particle types across different classifiers

Algorithm	Original dataset				Original dataset+generated dataset			
	Block	Sphere	Flake	Stick	Block	Sphere	Flake	Stick
K-NN	0.94	0.00	0.51	0.00	0.94	1.00	0.54	1.00
Random forest	0.89	0.00	0.73	0.00	0.89	1.00	0.73	1.00
TCBGY-Net	0.93	0.00	0.19	0.00	0.86	1.00	0.80	1.00
Proposed	0.89	0.00	0.87	0.00	0.89	1.00	0.90	0.97

remaining at 0.89. This is also the primary reason why the overall recognition accuracy of the proposed method only reached 0.90.

3.3 Wear evolution analysis of artificial joints based on particle recognition

Long-term simulation experiments were conducted to investigate the wear evolution of artificial joints. The experimental details of the friction pairs are provided in Section 2.1. The friction cycle count was set to five million friction cycles to cover three distinct wear states: running-in, steady wear, and severe wear. Wear particle samples were collected at intervals of one million friction cycles, and the captured images were automatically categorized into distinct types using the proposed particle recognition method. Additionally, the quantity and dimensional parameters of all particles were extracted to acquire wear particle distributions for wear evolution analysis of artificial joints.

3.3.1 Evolution analysis of wear conditions

Since particle size is an important factor reflecting wear conditions, the particle size distributions of different friction pairs are illustrated in Fig. 8. The figure shows a similar distribution of particle quantity generated from the CoCrMo–XLPE and PEEK–XLPE pairs. Most of the particles are less than 0.5 μm. In 1–3 million friction cycles, hardly any large particles (> 3 μm) are produced. As shown in Fig. 8(a), the particle quantity in 2 million friction cycles is the maximum and decreases to the minimum in 3 million friction cycles and then increases. These results indicate that the CoCrMo–XLPE pair is in the running-in period during 2 million friction cycles and in the steady wear period during 3 million friction cycles. In 5 million friction cycles, large particles are produced from the CoCrMo–XLPE pair, and the quantity increases, indicating that the wear condition becomes more severe.

As shown in Fig. 8(b), the quantity of wear particles generated from the PEEK–XLPE pair shows a downward trend in the first four stages (1–4 million friction cycles). This illustrates that the PEEK–XLPE pair is in the running-in period during 1 million friction cycles, which is earlier than that of the CoCrMo–XLPE pair. In the last two stages (4 and 5 million friction cycles), large particles are generated from the PEEK–XLPE pair, and the particle quantity in 5 million friction cycles is significantly increased. This indicates that the PEEK–XLPE pair enters a severe wear period after 4 million friction cycles. The investigation results are similar to those in our previous work [6].

3.3.2 Evolution analysis of the wear mechanism

Particle types are related to wear mechanisms, including abrasive wear, adhesion wear, cutting wear, and fatigue wear. The particle type distributions of different friction pairs at different friction cycles are shown in Fig. 9. Figure 9(a) shows that the block particles of the CoCrMo–XLPE pair occupy the main proportion (> 50%) throughout the wear process. The sphere particles increase from 23.4% at 1 million friction cycles to 32.6% at 2 million friction cycles, indicating that abrasive wear predominates at this wear stage. At 3 million friction cycles, the flack particles increase and occupy 13.2%, indicating that adhesive wear is produced. At 4 and 5 million friction cycles, the stick particles increase significantly, and the proportions are 11.5% and 15.8%, respectively. This result shows that the cutting wear caused by three-body abrasive wear is the main wear mechanism, and the wear condition becomes more severe.

Different from the CoCrMo–XLPE pair, the proportion of spherical particles of the PEEK–XLPE pair at 3 million friction cycles reaches 61.1%, as shown in Fig. 9(b). At this stage, the proportion of flack particles decreases to 2.2%. These results indicate that abrasive wear is the dominant wear mode, accompanied by plastic deformation of the material. At 4 million friction cycles, the spherical particles are missing, but the flack and

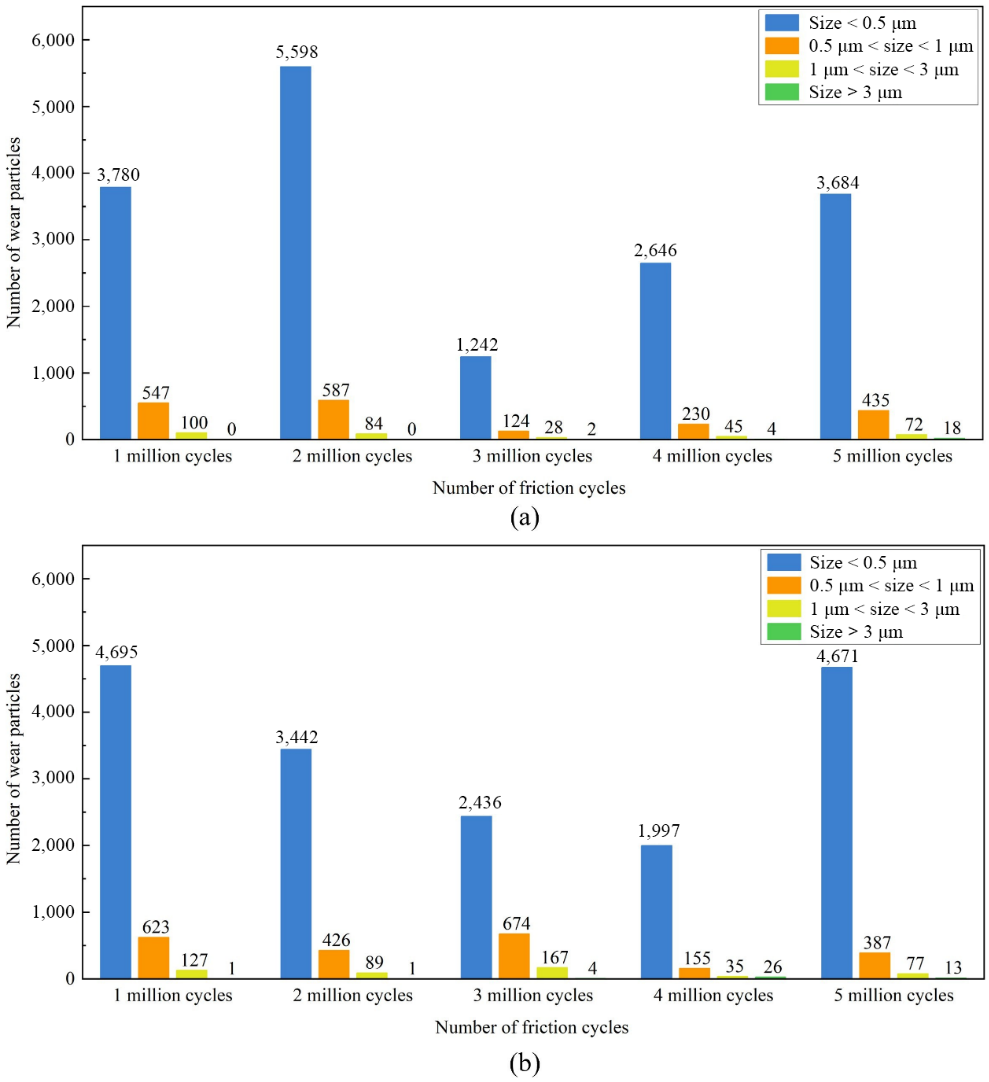

Fig. 8 Wear particle size distribution according to different friction cycles: (a) CoCrMo–XLPE and (b) PEEK–XLPE.

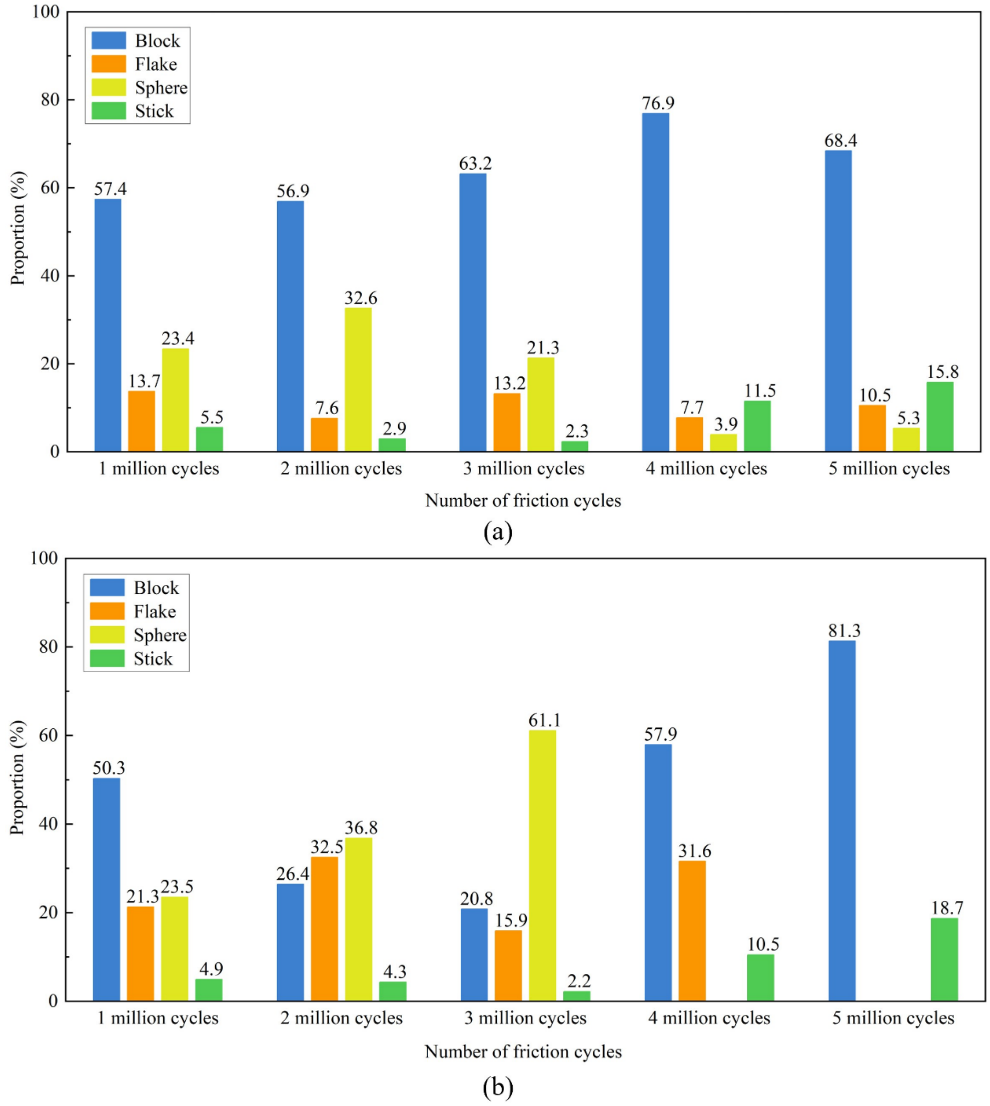

Fig. 9 Particle type distribution of different friction pairs at different friction cycles: (a) CoCrMo–XLPE and (b) PEEK–XLPE.

stick particles increase and occupy 31.6% and 10.5%, respectively, indicating that the adhesive wear is more significant. At 5 million friction cycles, only block and stick particles are captured, and the proportion of block particles reaches 81.3%. This indicates that the wear status enters a severe fatigue wear period along with cutting wear.

3.3.3 Comparison validation

To validate the reliability of the wear evolution analysis based on the wear particle distribution, the worn surfaces of friction pairs were imaged for contrast analysis. As shown in Fig. 10(a), the surface at 1 million friction cycles exhibits slight furrows that are caused by the cutting motion in abrasive wear. Then, the furrows become denser and deeper until 3 million friction cycles. At the same time, plastic deformation of the material occurs. Three-body abrasive wear is still the main wear mechanism. The appearance of spalling pits indicates that adhesive wear is produced and that the wear condition becomes severe. At 4 million friction cycles, the surface exhibits noticeable cracks and pits, indicating that adhesive wear becomes the main wear mode at this stage. It can be observed that the surface material is severely spalled at 5 million friction cycles. The furrows become more severe, and some block and stick particles are embedded in the worn surface. These phenomena result from both abrasive wear and adhesive wear.

As shown in Fig. 10(b), abrasive wear is the main wear mechanism on the PEEK–XLPE pair in the first 2 million friction cycles. At 3 million friction cycles, the surface shows plastic deformation and material spalling, and the grooves become denser and deeper, resulting from adhesive wear and severe cutting wear. At 4 and 5 million friction cycles, the embedded wear particles and the scratch morphology illustrate that the friction surface acts on both abrasive wear and adhesive wear. The wear condition in 5 million friction cycles becomes more severe.

In summary, the results of the evolution analysis on the wear condition and wear mechanism based on the wear particle distribution are similar to those using the worn surface morphologies. This verifies that our proposed method is effective for use in the wear evolution analysis of artificial joints. Moreover, the ability to acquire wear particles without prosthesis retrieval highlights the significant value of this method for wear condition analysis in joint implants.

4 Conclusions

For the purpose of wear evolution analysis of artificial joints, an intelligent wear particle recognition method is proposed to acquire the distribution for statistical analysis. To improve the particle recognition accuracy using insufficient and imbalanced samples, a

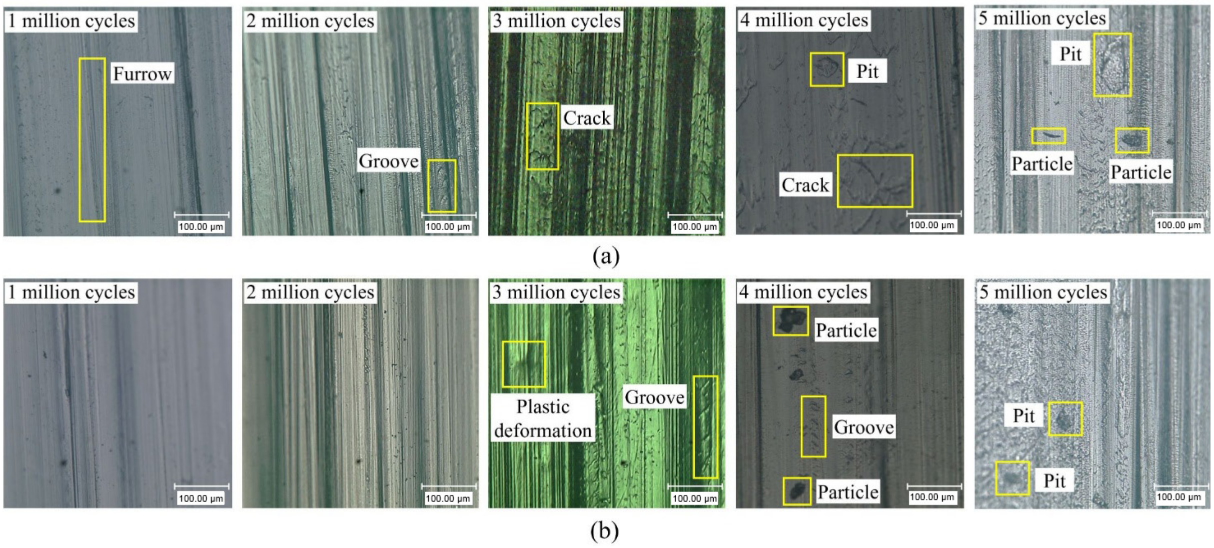

Fig. 10 Worn surfaces of different friction pairs at different friction cycles: (a) CoCrMo–XLPE and (b) PEEK–XLPE.

generative adversarial network is designed to expand the particle samples. The main conclusions are as follows:

(1) A wear particle generation network is designed with a multiscale coordinated attention module to improve the learning ability. A combined loss function is suggested to enhance the training stability and generate high-quality samples. The ablation experiment results verify the effectiveness of the generation network, whose performance metrics of SSIM, Ent_1, VoL, SF, IA, and FID reach 0.98, 0.97, 333.75, 13.88, 0.80, and 22.70, respectively. This performance outperforms the comparison methods of SAGAN, ProGAN, and StyleGAN3.

(2) An intelligent wear particle recognition model is built using an artificial neural network that is optimized with a learning rate annealing strategy and L2 regularization. The effectiveness of the optimization strategy is validated by an ablation experiment. After balancing the wear particle samples, the particle recognition accuracy, precision, recall, and F1-score are all increased to 0.90, which are higher than those of the comparison algorithms.

(3) Statistical analysis of wear particles is performed to obtain the particle size and type distribution. It is effective to analyze the evolution of the wear condition and wear mechanism of artificial joints. The experiments conducted with CoCrMo–XLPE and PEEK–XLPE friction pairs show that the particle size distribution has a relationship with the wear conditions, which can be used to identify the wear stages, including running-in, steady, and severe wear periods. The particle type distribution is helpful to analyze the wear mechanism evolution in abrasive, adhesive, fatigue, and cutting wear.

Acknowledgements

This work was supported in part by the National Natural Science Foundation of China (No. 52475205), the Natural Science Foundation of Guangdong Province (No. 2024A1515030208), the Shenzhen International Cooperation Research Project (No. GJHZ20220913143005009), the Development and Reform Commission of Shenzhen Municipality (No. XMHT20230115003), and the Electron Microscopy Center (EMC) of Shenzhen University.

Declaration of competing interest

The authors have no competing interests to declare that are relevant to the content of this article.

References

[1] Gelber A C. Knee osteoarthritis. *Ann Intern Med* **177**(9): ITC129–ITC144 (2024)

[2] Berteau J P. Systematic narrative review of modalities in physiotherapy for managing pain in hip and knee osteoarthritis: A review. *Medicine* **103**(39): e38225 (2024)

[3] Cen J J, Chen Q, Chen K, Zhang X Y, Feng H Y, Feng C A, Li X W, Zhang D K. Coupling mechanism of bioinspired artificial composite synovial fluid on the tribological behavior of artificial joints. *Friction* **13**(3): 9440908 (2025)

[4] Pu J, Zhang Z P, Zhang Y L, Zhang X G, Yuan X L, Zhang X Y, Zhang G X, Cui W, Yang S, Jin Z M. Fretting-corrosion mechanisms of Ti6Al4V against CoCrMo in simulated body fluid under various fretting states. *Friction* **12**(12): 2741–2759 (2024)

[5] Liu R J, Zhang Y L, Pu J, Jie M Y, Xiong Q, Zhang X G, Li X L, Jin Z M. Wear mechanism and wear debris characterization of ULWPE in multidirectional motion. *Tribol Lett* **72**(4): 130 (2024)

[6] Peng Y P, Kong D Y, Wang S, Cao G Z, Liu C Z. *In-vitro* investigation on the tribological properties of nickel–titanium (NiTi) alloy used in braided vascular stents. *Tribol T* **67**(5): 1002–1015 (2024)

[7] Nečas D, Usami H, Niimi T, Sawae Y, Křupka I, Hartl M. Running-in friction of hip joint replacements can be significantly reduced: The effect of surface-textured acetabular cup. *Friction* **8**(6): 1137–1152 (2020)

[8] Nayak S K, Hirwani J K, Sinha S K, Pandey R K. Mechanical and bio-tribological behaviours of UHMWPE based composites for prosthetic hip joint implant application. *Tribol Int* **199**: 109945 (2024)

[9] Thomas A D H, Davies T, Luxmoore A R. Computer image analysis for identification of wear particles. *Wear* **142**(2): 213–226 (1991)

[10] Peng Y P, Zhou Y Y, Wang S, Cao G Z, Liu C Z. Three-dimensional reconstruction of wear particle surfaces using multi-focus image sequence. *Measurement* **235**: 114925 (2024)

[11] Cen J J, Chen Q, Chen K, Zhang X Y, Feng H Y, Feng C N, Li X W, Zhang D K, Ge S R. Coupling influence between environmental factors and synovial fluid components on tribological behavior of hip joint materials. *Tribol Int* **204**: 110464 (2025)

[12] Hua Z K, Hu M D, Sheng B, Huang X L, Zhu J J, Jin Z M. Characteristics of VE/HXLPE wear particle morphology: A comparative analysis with UHMWPE in an *in vitro* artificial tibial insert simulation test. *Wear* **548**: 205390 (2024)

[13] Roylance B J, Raadnui S. The morphological attributes of wear particles—their role in identifying wear mechanisms. *Wear* **175**(1–2): 115–121 (1994)

[14] Kowandy C, Richard C, Chen Y M. Characterization of wear particles for comprehension of wear mechanisms: Case of PTFE against cast iron. *Wear* **265**(11–12): 1714–1719 (2008)
[15] Peng Y P, Yue H T, Wang S, Cao G Z, Wu H K, Liu C Z. Probability-weighted ensemble support vector machine for intelligent recognition of moving wear debris from joint implant. *Tribol Int* **186**: 108583 (2023)
[16] Hu X B, Song J, Liao Z H, Liu Y H, Gao J, Menze B, Liu W Q. Morphological residual convolutional neural network (M-RCNN) for intelligent recognition of wear particles from artificial joints. *Friction* **10**(4): 560–572 (2022)
[17] Li J H, Wang S, Fu S Q, Peng Y P. Study on wear debris characteristics of different polyethylene under reciprocating sliding and compound motion modes. *Wear* **530**: 205062 (2023)
[18] Peng Y P, Cai J H, Wu T H, Cao G Z, Kwok N, Zhou S X, Peng Z X. A hybrid convolutional neural network for intelligent wear particle classification. *Tribol Int* **138**: 166–173 (2019)
[19] Peng Y P, Cai J H, Wu T H, Cao G Z, Kwok N, Peng Z X. WP-DRnet: A novel wear particle detection and recognition network for automatic ferrograph image analysis. *Tribol Int* **151**: 106379 (2020)
[20] Wang S, Wan M, Wu T H, Bai Z C, Wang K P. Optimized Mask-RCNN model for particle chain segmentation based on improved online ferrograph sensor. *Friction* **12**(6): 1194–1213 (2024)
[21] Yin Y B, Zhang Q, Feng L, Song L, Wen Z H, Yuan Z, Wang M H. A wear debris recognition method based on dual-channel electrostatic signal and prominence of cross-correlation function. *Tribol Int* **190**: 109020 (2023)
[22] Liu Z Z, Zuo H F, Bai F, Liu Y, Dhupia J, Jia J J, Chen Z X. Intelligent classification of online wear particle in lubricating oil using optical direct imaging method and convolutional neural network for rotating machinery. *Tribol Int* **189**: 109015 (2023)
[23] He L, Wei H J, Sun C X. TCBGY net for enhanced wear particle detection in ferrography using self attention and multi scale fusion. *Sci Rep* **14**: 31549 (2024)
[24] Werner de Vargas V, Schneider Aranda J A, dos Santos Costa R, da Silva Pereira P R, Victória Barbosa J L. Imbalanced data preprocessing techniques for machine learning: A systematic mapping study. *Knowl Inf Syst* **65**(1): 31–57 (2023)
[25] Khan S H, Hayat M, Bennamoun M, Sohel F A, Togneri R. Cost-sensitive learning of deep feature representations from imbalanced data. *IEEE T Neur Net Lear* **29**(8): 3573–3587 (2018)
[26] Lin T Y, Goyal P, Girshick R, He K M, Dollár P. Focal loss for dense object detection. In: Proceedings of the IEEE International Conference on Computer Vision, 2017: 2999–3007.
[27] Montesinos López O A, Montesinos López A, Crossa J. Overfitting, model tuning, and evaluation of prediction performance. In: *Multivariate Statistical Machine Learning Methods for Genomic Prediction*. Cham: Springer, 2022: 109–139.
[28] Rezvani S, Wang X Z. A broad review on class imbalance learning techniques. *Appl Soft Comput* **143**: 110415 (2023)
[29] Chawla N V, Bowyer K W, Hall L O, Kegelmeyer W P. SMOTE: Synthetic minority over-sampling technique. *J Artif Intell Res* **16**: 321–357 (2002)
[30] He H B, Garcia E A. Learning from imbalanced data. *IEEE T Knowl Data En* **21**(9): 1263–1284 (2009)
[31] Chen Y Z, Yang X H, Wei Z H, Heidari A A, Zheng N G, Li Z C, Chen H L, Hu H G, Zhou Q W, Guan Q. Generative adversarial networks in medical image augmentation: A review. *Comput Biol Med* **144**: 105382 (2022)
[32] Sauer A, Chitta K, Müller J, Geiger A. Projected GANs converge faster. In: Proceedings of the 35th International Conference on Neural Information Processing Systems, 2021: 17480–17492.
[33] Zhang H, Goodfellow I, Metaxas D, Odena A. Self-attention generative adversarial networks. In: Proceedings of the 36th International Conference on Machine Learning, 2019: 7354–7363.
[34] Zhang X Y, Zhang T, Chen K, Xu H D, Feng C N, Zhang D K. Wear mechanism and debris analysis of PEEK as an alternative to CoCrMo in the femoral component of total knee replacement. *Friction* **11**(10): 1845–1861 (2023)
[35] Schnell T, Bott K, Puck L, Buettner T, Roennau A, Dillmann R. RoBiGAN: A bidirectional Wasserstein GAN approach for online robot fault diagnosis via internal anomaly detection. In: Proceedings of the IEEE/RSJ International Conference on Intelligent Robots and Systems, 2022: 4332–4337.
[36] Karthika S, Durgadevi M. Retraction Notice: Generative Adversarial Network (GAN): A general review on different variants of GAN and applications. In: Proceedings of the 6th International Conference on Communication and Electronics Systems, 2021.
[37] Raadnui S. Wear particle analysis—Utilization of quantitative computer image analysis: A review. *Tribol Int* **38**(10): 871–878 (2005)
[38] Yue H T, Peng Y P, Wang S, Cao G Z, Li H P. Intelligent recognition of artificial joint wear particles from lubrication fluid based on multi-view image features. In: Proceedings of the 6th International Conference on Biomedical Engineering and Applications, 2022: 32–39.
[39] He K M, Zhang X Y, Ren S Q, Sun J. Delving deep into rectifiers: Surpassing human-level performance on ImageNet classification. In: Proceedings of the IEEE International Conference on Computer Vision, 2015: 1026–1034.
[40] He K M, Zhang X Y, Ren S Q, Sun J. Deep residual learning for image recognition. In: Proceedings of the IEEE Conference on Computer Vision and Pattern Recognition, 2016: 770–778.
[41] Pongrac B, Gleich D. Despeckling of SAR images using residual twin CNN and multi-resolution attention mechanism. *Remote Sens* **15**(14): 3698 (2023)
[42] Chaabane F, Réjichi S, Tupin F. Self-attention generative adversarial networks for times series VHR multispectral image generation. In: Proceedings of the IEEE International Geoscience and Remote Sensing Symposium, 2021: 4644–4647.
[43] Speck D, Rosin T P, Kerzel M, Wermter S. The importance of growing up: Progressive growing GANs for image inpainting. In: Proceedings of the IEEE International Conference on Development and Learning, 2023: 294–299.
[44] Karras T, Aittala M, Laine S, Härkönen E, Hellsten J, Lehtinen J, Aila T. Alias-free generative adversarial networks. In: Proceedings of the 35th International Conference on Neural Information Processing Systems, 2021: 852–863.

Yeping Peng received her Ph.D. degree in mechanical engineering from Xi'an Jiaotong University, China, in 2017. She is currently an associate professor at the Guangdong Key Laboratory of Electromagnetic Control and Intelligent Robots, College of Mechatronics and Control Engineering, Shenzhen University, China. She has published more than 60 journal articles and conference papers. Her main research interests include tribology, condition monitoring, and wear analysis.

Song Wang received his Ph.D. degree from Tsinghua University, China, in 2015. He has been an associate researcher at the Research Institute of Tsinghua University in Shenzhen, China, since 2015. His current research interests cover orthopedic biomaterials, biotribology, and medical devices. He has published more than 80 academic papers and applied for over 40 Chinese patents. He also serves as an external graduate advisor at Tsinghua University, Sun Yat-sen University, and Shenzhen University, China, and holds positions as a member of several professional associations in the industry.

Guang-Zhong Cao received his Ph.D. degree in electrical engineering and automation from Xi'an Jiaotong University, China, in 1996. He is currently a professor and the director of the Guangdong Key Laboratory of Electromagnetic Control and Intelligent Robots, Shenzhen University, China. He has authored more than 100 articles published in refereed journals and conference proceedings. His research interests include control theory, image processing, and information processing.